Available online at www.sciencedirect.com
SCIENCE DIRECT®
Comput. Methods Appl. Mech. Engrg. 192 (2003) 4173–4193
Computer methods in applied mechanics and engineering
www.elsevier.com/locate/cma

A novel approach of three-dimensional hybrid grid methodology: Part 2. Flow solution

Meng-Sing Liou, Yao Zheng *

NASA Glenn Research Center, MS 5-11, 21000 Brookpark Road, Cleveland, OH 44135, USA

Received 13 August 2001; received in revised form 22 April 2003; accepted 21 May 2003

Abstract

Following the previous paper of this series, which addresses the generation approach of three-dimensional DRAGON grids, we demonstrate the capability of effectively performing three-dimensional flow calculations for multi-components complex configurations. The flow solution is conducted by means of using a seamlessly integrated package made up of two well-validated NASA solvers, which are structured- and unstructured-grid codes, respectively.

Keywords: Computational fluid dynamics; Flow solution; AUSM scheme; Hybrid grid; Turbomachinery; Turbine vanes; Cascade flow; Supersonic flow; Subsonic flow; Viscous flow

1. Introduction

In the previous paper of this series [14], we have presented the essentials and challenges of a novel three-dimensional hybrid grid, termed DRAGON grid, methodology [10,11,13,15]. The DRAGON grid scheme is capable of completely eliminating the interpolation and preserving the flux conservation property. It adapts and maximizes the advantages of both structured and unstructured grids, while at the same time it eliminates the weaknesses of the Chimera scheme and minimizes the memory requirement associated with the unstructured grid.

The present work is to develop a flow solver devoted to the computational fluid dynamics (CFD) simulation using DRAGON grid technology in the three-dimensional space [10–13]. The resulting program suite is named as DRAGONFLOW. It is the result of integrating works of other researchers, and it is adopted and redesigned from two existing successful flow solvers OVERFLOW [1] and USM3D [4,5]. OVERFLOW is a Navier–Stokes code working with Chimera grid, and is used here to solve flow problems on the domain occupied by composite structured grids of a DRAGON grid. USM3D solves Navier–Stokes

* Corresponding author. Present address: Center for Engineering and Scientific Computation, and College of Computer Science, Zhejiang University, Hangzhou, Zhejiang 310027, PR China.
E-mail addresses: meng-sing.liou-1@nasa.gov (M.-S. Liou), yao.zheng@zju.edu.cn, yao.zheng@computer.org (Y. Zheng).

0045-7825/$ - see front matter
doi:10.1016/S0045-7825(03)00386-4

equations on an unstructured tetrahedral grid, and is employed to perform flow simulation over a collection of unstructured grids of a DRAGON grid.

2. Solution scheme

2.1. Governing equations

The time-dependent compressible Navier–Stokes equations given by Eq. (1), in an integral form over an arbitrary control volume Ω, are solved:

$$\int_{\Omega} \frac{\partial \mathbf{U}}{\partial t} \, \mathrm{d}v + \int_{\partial\Omega} \vec{\mathbf{F}} \cdot \mathrm{d}\vec{S} = 0, \tag{1}$$

where the conservative-variable vector $\mathbf{U} = (\rho, \rho u, \rho v, \rho w, \rho e_t)^{\mathrm{T}}$, with the specific total energy $e_t = e + |\vec{V}|^2/2 = h_t - p/\rho$. The flux vector $\vec{\mathbf{F}}$ includes both the inviscid and viscous fluxes, in which the turbulence variables are also included. We denote with an overhead arrow the vector quantities expressed in terms of Cartesian coordinates.

2.2. Flux splitting

Based on the cell-centered finite volume method, the governing equations are semi-discretized. We use the flux scheme AUSM$^+$, described in full detail in [7], to express the numerical inviscid flux at the cell faces. The basic idea of AUSM$^+$ follows that of its predecessor, AUSM [9], but has substantial improvements. The AUSM$^+$, incurring negligible additional cost over the earlier AUSM scheme, allows exact capture of a normal shock by using a suitably chosen interface speed of sound, yields a smoother solution by utilizing higher-order polynomials, and often results in a faster convergence rate.

The semi-discretized form, describing the time rate of change of $\mathbf{U}$ in Ω via balance of fluxes through all enclosing faces, $\vec{S}_l$, $l = 1, \ldots, LX$, independent of whether they are in the structured or unstructured grid regions, can be cast as

$$\int_{\Omega} \frac{\partial \mathbf{U}}{\partial t} \, \mathrm{d}v + \sum_{l=1}^{LX} \vec{\mathbf{F}}_l \cdot \vec{S}_l = \int_{\Omega} \frac{\partial \mathbf{U}}{\partial t} \, \mathrm{d}v + \sum_{l=1}^{LX} \mathbf{F}_{nl} |\vec{S}_l| = 0. \tag{2}$$

Noting that the flux terms account for only normal components of the flux at the face, $\mathbf{F}_{nl} = \vec{\mathbf{F}}_l \cdot \vec{n}_l$ where $\vec{n}_l$ is the unit normal vector of $\vec{S}_l$. The task is then to represent the numerical flux at the cell interface $\vec{S}_l$, which straddles cells denoted by subscripts "L" and "R". The AUSM$^+$ scheme gives the numerical flux in the following expression.

$$\mathbf{F}_{nl} = M_l \frac{a_l}{2} (\mathbf{\Phi}_{\mathrm{L}} + \mathbf{\Phi}_{\mathrm{R}}) - |M_l| \frac{a_l}{2} \Delta\mathbf{\Phi} + \mathbf{P}_{nl}. \tag{3}$$

We remark that there is enough freedom for defining the interface speed of sound a_l so that certain criteria are met [7,8]. An interesting notion is the so-called numerical speed of sound, which is introduced to handle low Mach number flows and later is extended to the multiphase flows [8]. The interface Mach number M_l is an important variable and defined in the following steps.

1. Project velocity vectors at the cell centers, "L" and "R", to $\vec{S}_l$,

$$V_{\mathrm{L}} = \vec{V}_{\mathrm{L}} \cdot \vec{n}_l, \qquad V_{\mathrm{R}} = \vec{V}_{\mathrm{R}} \cdot \vec{n}_l. \tag{4}$$

2. Define the corresponding Mach numbers,
$$M_{\mathrm{L}} = \frac{V_{\mathrm{L}}}{a_l}, \qquad M_{\mathrm{R}} = \frac{V_{\mathrm{R}}}{a_l}. \tag{5}$$
3. Define the interface convective Mach number by writing
$$M_l = \mathscr{M}^{+}_{(4)}(M_{\mathrm{L}}) + \mathscr{M}^{-}_{(4)}(M_{\mathrm{R}}), \tag{6}$$
where the formulas for $\mathscr{M}^{\pm}_{(4)}$ are expressed in terms of eigenvalues of the nonlinear waves, $M+1$ and $M-1$ [7].
$$\mathscr{M}^{\pm}_{(4)}(M) = \begin{cases} \frac{1}{2}(M \pm |M|) & \text{if } |M| \geqslant 1, \\ \mathscr{M}^{\pm}_{(2)}(1 \mp 2\mathscr{M}^{\mp}_{(2)}) & \text{otherwise,} \end{cases} \tag{7}$$
where
$$\mathscr{M}^{\pm}_{(2)}(M) = \pm\tfrac{1}{4}(M \pm 1)^2. \tag{8}$$
4. Define the interface pressure p_l in terms of the above-defined Mach numbers,
$$p_l = \mathscr{P}^{+}_{(5)}(M_{\mathrm{L}})p_{\mathrm{L}} + \mathscr{P}^{-}_{(5)}(M_{\mathrm{R}})p_{\mathrm{R}}, \tag{9}$$
where similarly we use the following polynomials,
$$\mathscr{P}^{\pm}_{(5)}(M) = \begin{cases} \frac{1}{2M}(M \pm |M|) & \text{if } |M| \geqslant 1, \\ \mathscr{M}^{\pm}_{(2)}[(\pm 2 - M) \mp 3M\mathscr{M}^{\mp}_{(2)}] & \text{otherwise.} \end{cases} \tag{10}$$
Then, we get
$$\mathbf{P}_{nl} = p_l \begin{pmatrix} 0 \\ n_{lx} \\ n_{ly} \\ n_{lz} \\ 0 \end{pmatrix}. \tag{11}$$
5. Assemble the interface numerical flux by inserting $(M_l, \mathbf{P}_{nl})$ in Eq. (3).

2.3. Flow solvers

As mentioned before, the flow code DRAGONFLOW is made up of two well-validated NASA codes, OVERFLOW [1] and USM3D [5], which are respectively structured- and unstructured-grid codes. We have spent a significant effort to add an interface and modify both codes, more so for the OVERFLOW code. The interested readers should consult with the cited references for details of either code. The details on implementing the DRAGONFLOW code are to be addressed in the next section. Nonetheless, there are differences between these codes that warrant concerns and cares when combining them into the present framework, such as time integration schemes, order of spatial discretizations, and choice of turbulence models.

A spatial-factored implicit algorithm is employed in the OVERFLOW code, while a point implicit one in the USM3D code. Since we are only interested in seeking steady state solutions, the differences of convergence rate due to the incompatibility between the structured and unstructured grid regions can be tolerated. However, if unsteady solutions are of interest, this difficulty can be overcome by a dual time integration approach in which the solution within each physical time step will be iterated to achieve convergence. This subject is left for a future research.

As for the spatial discretization, there is inconsistency in the order of accuracy in that a third-order and a second-order accurate schemes are used respectively in the structured grid-based and unstructured grid-based codes. But in both cases a similar limiter function is applied. We use the aforementioned flux scheme AUSM$^+$ to express the inviscid flux at the cell faces in both the OVERFLOW and USM3D codes. Also, the viscous fluxes are approximated, as usual, by a centered scheme.

3. Implementation of the flow code

3.1. Generic concept of data communication through grid interfaces

In the Chimera method, communication through grid interfaces is made through the hole boundary or the outer boundary. Since the interface treatment methods are not necessarily satisfying any form of conservative constraints, the solutions on overlaid grids are often mismatched with each other. More seriously, this may ultimately lead to spurious or incorrect solutions, especially when a shock wave or high-gradient region passes through boundaries of overlaid grids, as will be seen later.

For the DRAGON grid, conservation laws are solved on the same basis on both the structured and unstructured grids. Fig. 1 shows an interface connecting both structured and unstructured grids, assuming the cell center scheme is used. As described earlier, the numerical fluxes, evaluated at the cell interface, are based on the conditions of neighboring cells (denoted as L and R cells, respectively). For the unstructured grid, the interface flux $\mathbf{F}_{nl}$, will be evaluated using the structured-cell value as the right (R) state and the unstructured-cell value as the left (L) state. Consequently, the interface fluxes, which have been evaluated for the unstructured grid, can now be directly applied in computing the cell volume residuals for the structured grid.

Thus, the data communication through grid interfaces in the DRAGON grid guarantees satisfying of the conservation laws. It is considered seamless in the sense that no manipulation of data, which introduces uncertainties, is required, and the solution is obtained on the same basis for both structured and unstructured grid regions. Consequently this strictly enforces the conservation property locally and globally.

3.2. Fictitious structured grids

In Fig. 1, the cell center scheme is assumed for both structured and unstructured grids. However, the OVERFLOW code used in the structured grid regions is developed based on a nodal-based scheme, where

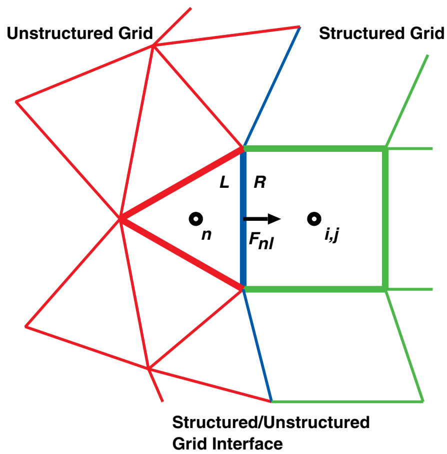

Fig. 1. Fluxes at the cell face connecting the structured and unstructured grids.

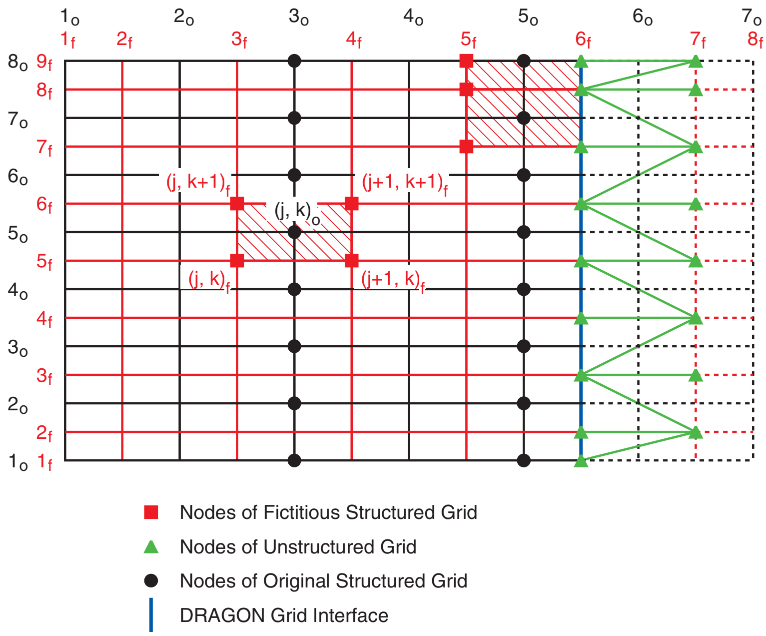

Fig. 2. Diagram of a fictitious grid associated with its original structured grid.

the flow variables are solved and stored at the grid points, rather than being offset to the center of the cells defined by the grid points. The surface of the unstructured grids within interfacial areas between the two types of grids could not match a surface described by nodes in the structured grids, in order to establish reasonable data communication through grid interfaces. For the DRAGONFLOW code, special treatment has been proposed to tackle the difficulty associated with the difference between cell-based and node-based schemes. This can be neatly resolved by a novel use of fictitious structured grids based on the original structured grids.

From a structured grid with $l \times m \times n$ nodes, an artificial grid with $(l+1) \times (m+1) \times (n+1)$ nodes can be constructed by means of introducing middle nodes between original nodes. It is clear that the new grid is shifted from the original one by a half cell size in the interior of the original grid. This new grid is referred to as a fictitious grid, and the associated nodes are named as fictitious nodes. Fig. 2 gives an illustration of the fictitious grid. Cell center (j,k), which is node $(j,k)_{\mathrm{o}}$ of the original grid, is surrounded by nodes $(j,k)_{\mathrm{f}}$, $(j+1,k)_{\mathrm{f}}$, $(j+1,k+1)_{\mathrm{f}}$ and $(j,k+1)_{\mathrm{f}}$ of the fictitious grid. Subscripts "o" and "f" denote "original" and "fictitious" grids, respectively.

3.3. Establishing DRAGON grid interfaces

It is obvious that the faces described by the fictitious nodes are the faces of finite volumes centered at the original nodes. For the fictitious grids, if we mimic the gridding method of DRAGON grids based on the original structured grids, as proposed in Ref. [15], then we can generate a DRAGON grid based on the fictitious grids. Moreover, the DRAGON interfacial boundary nodes of the unstructured grid coincide with the corresponding nodes on the fictitious grid. Because the numerical fluxes are still conservative in the DRAGON grid interface, the conservation property will not be affected by means of using a fictitious grid.

During the creation of the DRAGON grid based on the fictitious grids, IBLANK values for the fictitious grids can be automatically specified, taking into account the IBLANK values of the original grids.

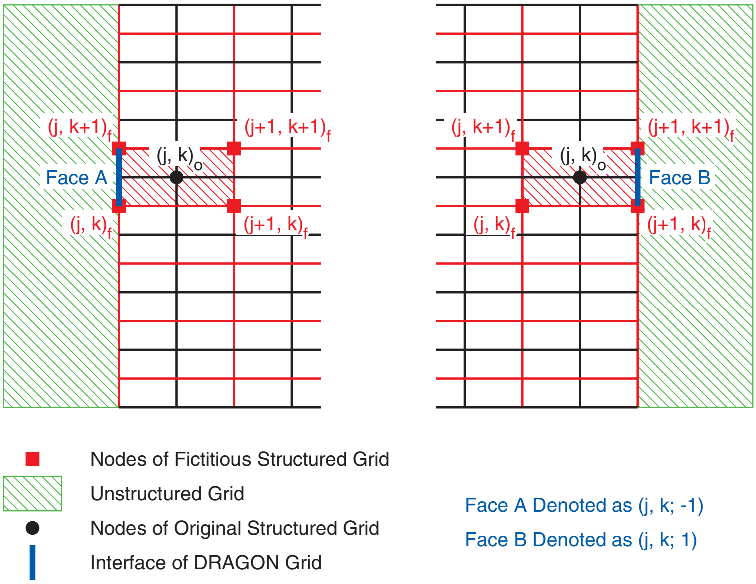

Fig. 3. Diagram of 2D DRAGON grid interfaces.

A fictitious node is specified 1 as its IBLANK value, if and only if there is an original node nearby with IBLANK value 1.

The faces of DRAGON grid interface are constructed from certain faces of the finite volumes centered at the original nodes. For an original node of interest, there are six possible faces, which could become faces of the DRAGON grid interface. Fig. 3 illustrates the numbering systems of the original grid, fictitious grid and flux definition, given Faces A and B as possible faces of the DRAGON grid interface, within a frame of a two-dimension problem. In this case, Faces A and B are defined as $(j,k;-1)$ and $(j,k;1)$, where ± 1 denotes the directions of the face. For Face A (idir $= -1$), $(j,k;-1)$ represents the index of cell center j_o, flux $(j-1)_\mathrm{fl}$ at the $j-1$ face and the fictitious grid index j_f. While for Face B (idir $= 1$), $(j,k;1)$ represents the index of cell center j_o, flux j_fl at the j face and the fictitious grid index $(j+1)_\mathrm{f}$. Generally, for three-dimensional cases, the notation of face directions is given in Fig. 4.

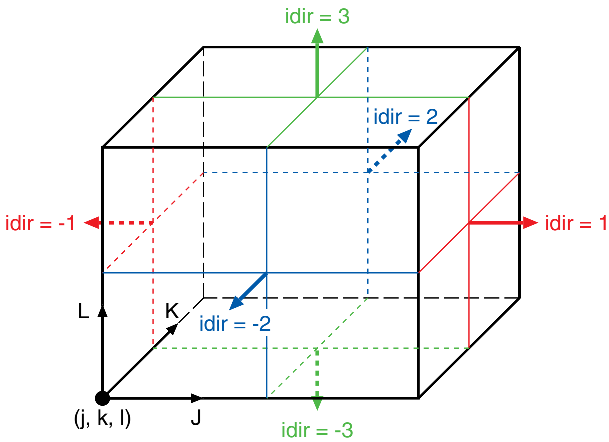

Fig. 4. Notation of face directions of 3D DRAGON grid interfaces.

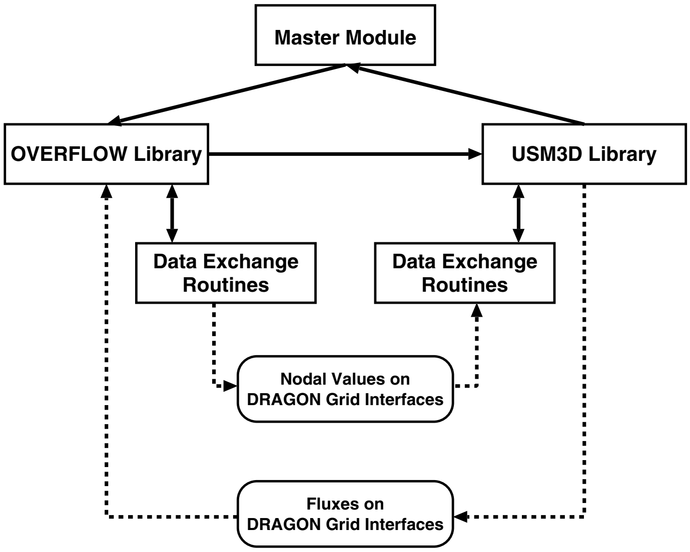

Fig. 5. Flowchart of the DRAGONFLOW procedure.

In the DRAGONFLOW procedure, values of nodal variables of structured grids near the interfaces are passed to the counterpart in the side of unstructured grids. These values are used to compute flux values on the interfaces. Therefore, the information from the side of structured grids contributes to the evolution of the solution in the unstructured grid regions. On the other hand, the fluxes computed are passed to the OVERFLOW to influence the solution in the structured grid regions.

3.4. Programming philosophy

The adoption of OVERFLOW and USM3D codes for the DRAGON grid is based on the concept of domain splitting. A DRAGON grid is dealt with as a combination of a Chimera grid and a collection of unstructured grids. In the DRAGONFLOW suite, both OVERFLOW and USM3D are presented in form of module libraries, and a master module controls the invoking of these individual modules. The alternative invoking of these solvers in each time step, and the immediate data exchange on the DRAGON grid interfaces, leads to a seamless coupling of these two solvers. Fig. 5 depicts the flow chart of the DRAGONFLOW suite. A significant effort has been made to add an interface and modify both codes, more so on the OVERFLOW code.

4. Benchmark tests

4.1. Shock tube problem

First, a 2D shock tube problem was considered. To focus only on the issue of grids, the flow was solved by the basic first-order accurate discretization in both time and space. This case serves to show the effect of interpolation in the Chimera grid and the validity of the DRAGON grid method for a transient problem as a plane shock moves across the embedded-grid region. The shock wave is moving into a quiescent region in a constant-area channel with a designed shock speed $M_s = 4$. Solutions were obtained using three grid

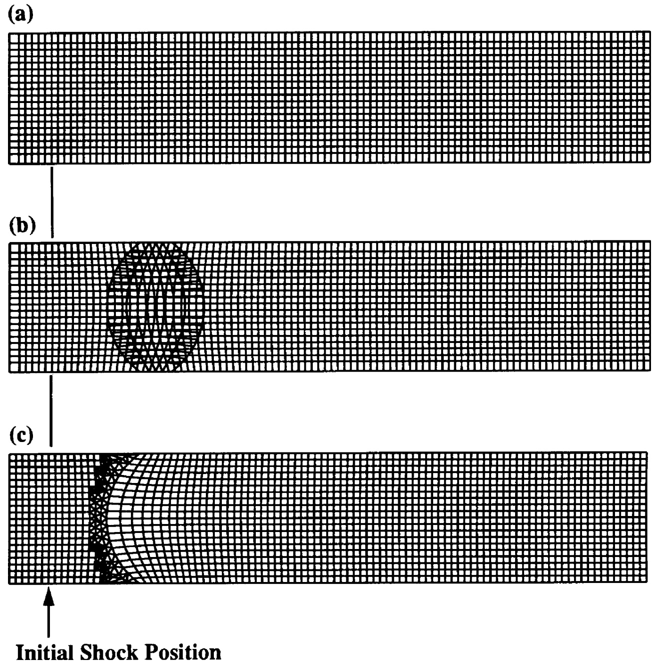

Fig. 6. Grids for moving shock problem ($M_s = 4$): (a) single grid, (b) Chimera grid, and (c) DRAGON grid.

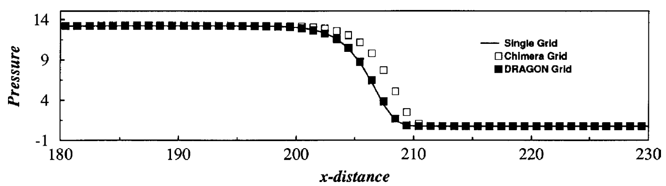

Fig. 7. Comparison of centerline pressures from the three grids.

systems, namely (1) single grid, (2) Chimera grid, and (3) DRAGON grid, as displayed in Fig. 6. The single grid solution is used for benchmark comparison.

The pressure distributions along the centerline of the channel, as plotted in Fig. 7, shows that the Chimera scheme predicts a faster moving shock in the tube, while the present DRAGON grid and the single grid results coincide, indicating that the shock is accurately captured and conservation property well preserved when going through the region of the embedded DRAGON grid.

4.2. 2D supersonic flow in a symmetric convergent channel

Now we consider a supersonic flow of Mach 1.8 through a symmetric convergent channel. The configuration and pressure pattern are sketched in Fig. 8, where both the top and bottom walls are bent, thus creating two wedge shocks of equal strength. The wedge angle is sufficiently large so that there is a Mach stem after the interaction of the two wedge shocks, resulting in a subsonic flow there. However, the exit flow is still supersonic, due to the acceleration of the fans emitting from the shoulders of the steps.

This test case is designed to provide a comparison in terms of conservation property between Chimera and DRAGON grids. The problem has been solved by using a single grid, two Chimera grids and a

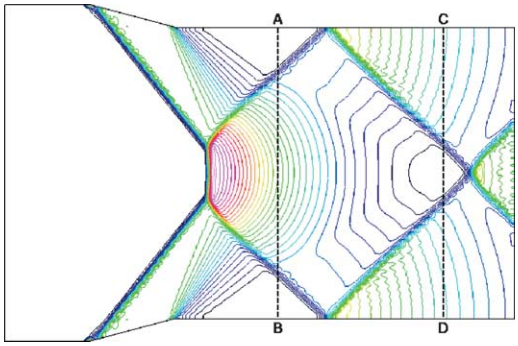

Fig. 8. Geometry and pressure pattern of a symmetric convergent channel, through which a supersonic flow is passing.

DRAGON grid, respectively. This configuration is treated as a three-dimensional geometry. Grids are generated to fill the whole domain, although the geometry is symmetric. Fig. 9(a) depicts the pressure contours of the flow computed based on the single grid. Fig. 9(b) and (c) show those computed based on two Chimera grids I and II. The Chimera grids I and II have the same grid point distributions as the single grid, apart from the overlapping areas. The nodal points in the overlapping areas are modestly displaced from those identical to the single grid. The difference between the Chimera grids I and II is due to the locations of the overlapping areas. Chimera grid II shown in Fig. 9(c) is constructed in such a way that a segment of shock almost lies on one of the grid boundary. This could be the worst case that causes a large error in the simulation. However, Chimera grid I shown in Fig. 9(b) could be considered as a typical one for general applications of Chimera grids. Fig. 9(d) depicts the pressure contours of the flow computed based on a DRAGON grid. This DRAGON grid is constructed based on Chimera grid II, and a segment of shock almost lies on the DRAGON grid interface. In Fig. 9(d), the contours are plotted based on the original structured grids and the corresponding unstructured grid forming the DRAGON grid. Therefore, there are discontinuities in the contour plot near the DRAGON grid interface, as there are gaps of a half cell size between the original structured grids and the unstructured grid.

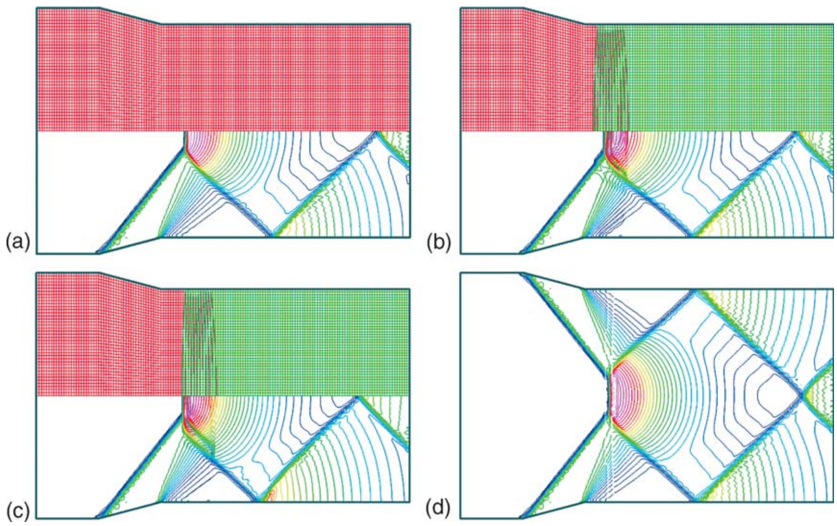

Fig. 9. Pressure contours of the flow: (a) Single grid, (b,c) Chimera grids I and II, and (d) DRAGON grid.

Fig. 10 presents the computed pressure distributions on Lines AB and CD, referring to Fig. 8. It confirms that variable interpolation between grids of a Chimera grid causes the loss of conservative property, and could introduce globally significant errors in some cases. However, the DRAGON grid scheme overcomes this shortcoming.

4.3. 3D supersonic flow in a convergent duct with two bent side walls

Next we consider a supersonic flow of Mach 3 through a convergent channel. The geometry is sketched in Fig. 11, where both the top and front side walls are bent by a wedge angle of 10°, thus creating two wedge shocks of equal strength and subsequent interactions between them. A strip of unstructured-gridded region, denoted by the shaded region, is placed in the mid-section of the channel. This test case is designed to provide a check on the three-dimensional code against conservation property of the DRAGON grid through a shock. The flow consists of two planar wedge shocks, two embedded shocks, a corner shock and two shear lines (slip surfaces) as shown in Fig. 12, where the location of Section IJKL is depicted in Fig. 11. The two wedge shocks intersect and generate, near the corner edge AD (see Fig. 11), a corner shock region manifested by the slip surfaces emanating from the triple point. Fig. 13 displays the density contours on the top and front side faces, and the exit plane. As seen in Figs. 14 and 15, the corner shock region progressively becomes larger as the wedge shocks sweep towards the opposite walls. Eventually these two wedge shocks reflect and interact with the flow previously generated by the corner shocks, making the flow field even more complicated.

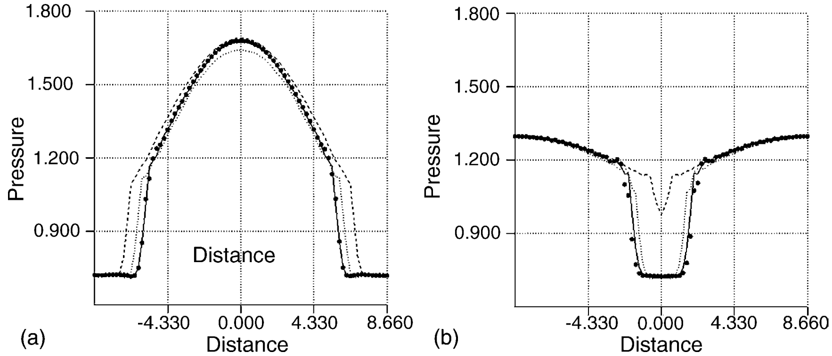

Fig. 10. Pressure distributions of the flow on Lines AB (a) and CD (b), referring to Fig. 8. Solid, dotted, dashed lines and circles denote results based on the single grid, Chimera grids I and II, and the DRAGON grid, respectively.

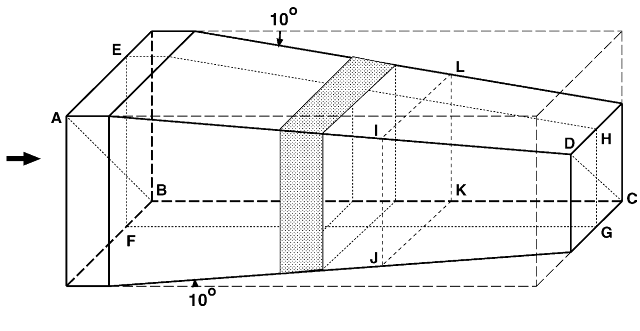

Fig. 11. Sketch of a convergent duct where the unstructured grid is in the shaded region for the DRAGON grid.

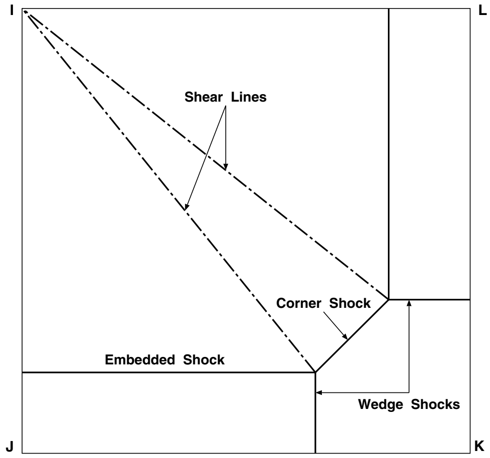

Fig. 12. Flow structure in Section IJKL of the supersonic flow passing a convergent duct.

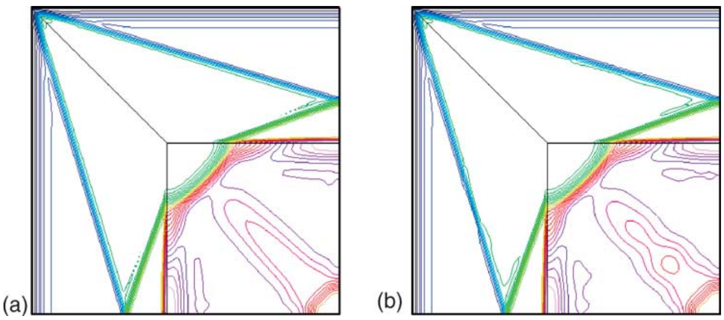

Fig. 13. Density distributions of the flow on the surface of the convergent duct: (a) single grid and (b) DRAGON grid.

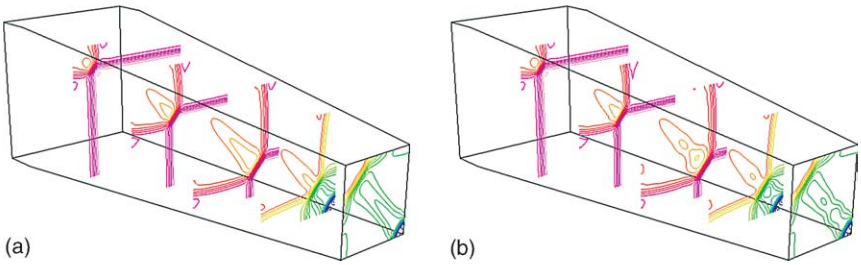

Fig. 14. Mach number distributions of the flow at various stations: (a) single grid and (b) DRAGON grid.

In Figs. 16–18, we give an inside view of variables on two planes: density contours on the symmetric plane ABCD (as denoted in Fig. 11), and Mach number and pressure contours on the midplane EFGH. This reveals quite a rich feature of shock-shock interactions inside the duct, while the shock configuration on the duct walls (Fig. 13) is relatively simple. The slip surfaces issuing from the shock triple points are evident in Fig. 17 and they subsequently interact with the downstream shock.

It is evident that the shock profiles pass through the DRAGON grid interfaces seamlessly without creating spurious waves, guaranteeing the conservation property. In each of the above figures, we also

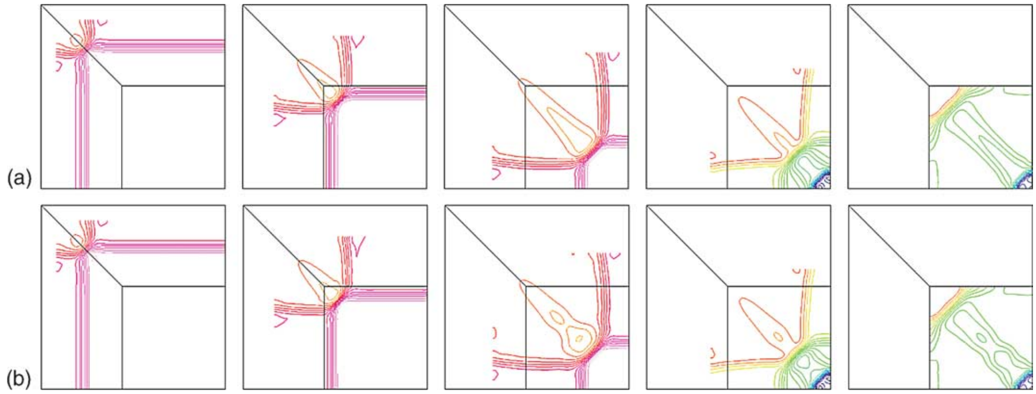

Fig. 15. Mach number distributions of the flow at various stations (split view): (a) single grid and (b) DRAGON grid.

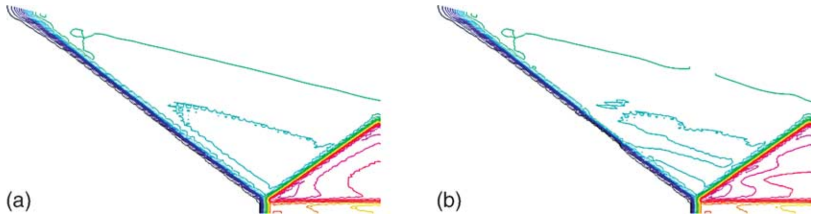

Fig. 16. Density distributions of the flow at the symmetric plane ABCD: (a) single grid and (b) DRAGON grid.

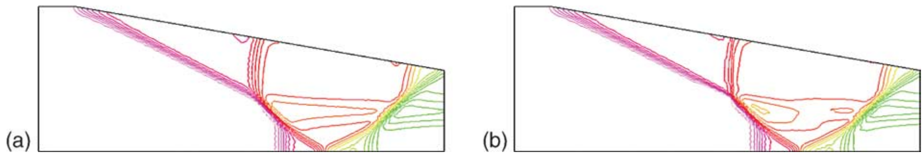

Fig. 17. Mach number distributions of the flow at a typical cutting plane EFGH: (a) single grid and (b) DRAGON grid.

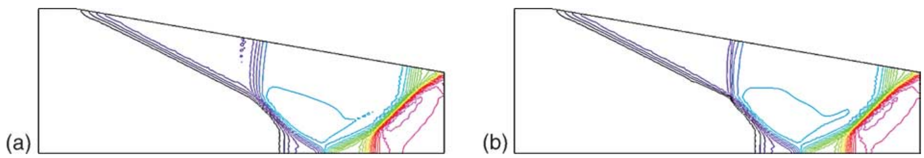

Fig. 18. Pressure distributions of the flow at a typical cutting plane EFGH: (a) single grid and (b) DRAGON grid.

include the results based on a single structured grid for validation. We see that both sets of results are essentially the same, except some minute variations in the core region, which are a remanent result of the unstructured grid. This is clearly indicated in Fig. 16 where the shock becomes thinner in the unstructured grid region because the grid size is reduced roughly by 1/6. A quantitative measure of the difference between the single grid and DRAGON grid solutions at the exit plane is given in Fig. 19, indicating a close agreement of the two solutions.

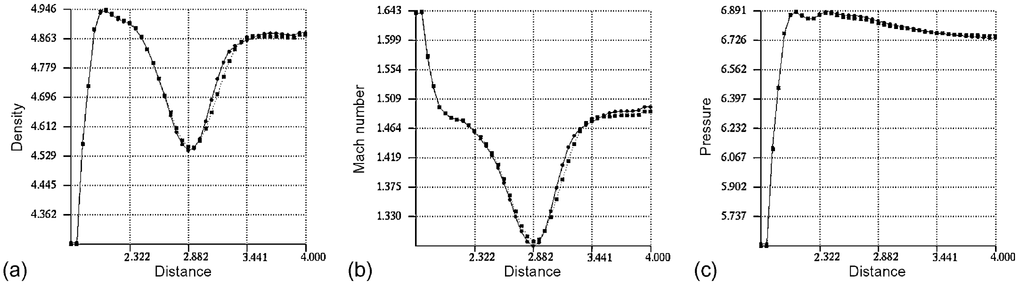

Fig. 19. (a) Density, (b) Mach number and (c) pressure distributions of the flow on Line HG. Boxes and circles denote results based on the single grid and the DRAGON grid, respectively.

4.4. Subsonic flow through a wavy-wall duct

We consider a subsonic flow in a wavy-wall duct. This test case is designed to provide a check on the three-dimensional code against conservation property of the DRAGON grid for a subsonic flow. We have performed computational simulation based on a single grid and a DRAGON grid, respectively. The DRAGON grid has unstructured grid regions of a shape as Label "3D", and the geometry is sketched in Fig. 20. Fig. 21 provides additional views of the DRAGON grid. As the result, Figs. 22–24 depict the

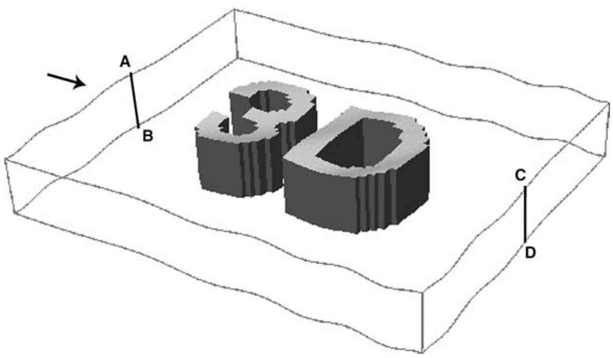

Fig. 20. Sketch of a wavy-wall duct where the unstructured grid is in the shaded region for the DRAGON grid.

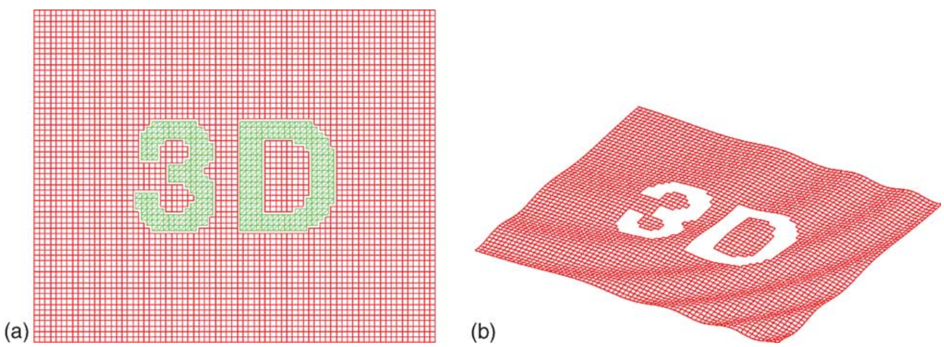

Fig. 21. (a) View of the DRAGON grid and (b) layer of the structured grid in the DRAGON grid.

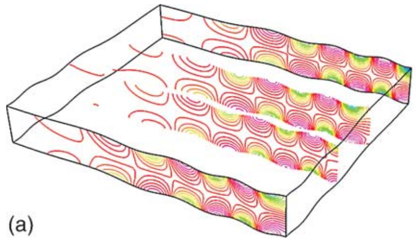

Fig. 22. Density distributions of the flow in the wavy-wall duct: (a) single grid and (b) DRAGON grid.

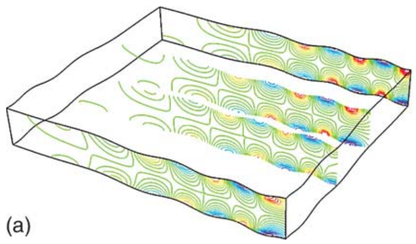

Fig. 23. Mach number distributions of the flow in the wavy-wall duct: (a) single grid and (b) DRAGON grid.

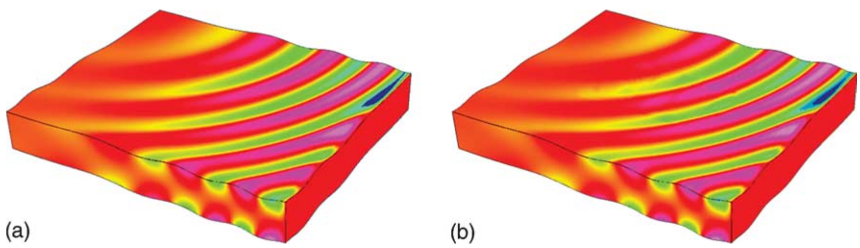

Fig. 24. Pressure distributions of the flow on the surface of the wavy-wall duct: (a) single grid and (b) DRAGON grid.

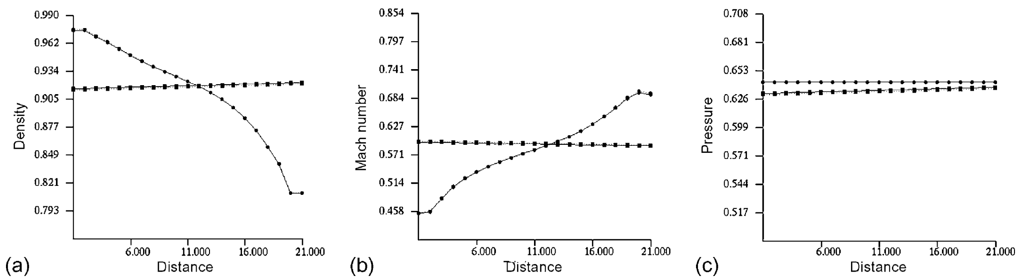

Fig. 25. (a) Density, (b) Mach number and (c) pressure distributions of the flow on Lines AB (boxes) and CD (circles). Doted and solid lines denote results based on the single grid and the DRAGON grid, respectively.

density, Mach number and pressure distributions for both cases based on the single grid and the DRAGON grid. It is evident that the results of both cases are essentially the same. The flow passes through the

DRAGON grid interfaces seamlessly without creating spurious diffusion, and this guarantees the conservation property.

And further, Fig. 25 shows a quantitative measure of the difference between the single grid and DRAGON grid solutions on lines AB and CD, which are defined in Fig. 20. This figure indicates a close agreement of the two solutions in terms of density, Mach number and pressure distributions.

5. Numerical simulations

5.1. Inviscid flow around a linear cascade

We have conducted a 3D calculation of an inviscid flow around a cascade in a turning duct. This solution exhibits the capability of DRAGON grid scheme in dealing with problems involving complex geometries. Also calculation based on a Chimera grid, which is the base grid of the DRAGON grid, has been conducted in order to make a comparison. Fig. 26 illustrates the 3D DRAGON and Chimera grids for the

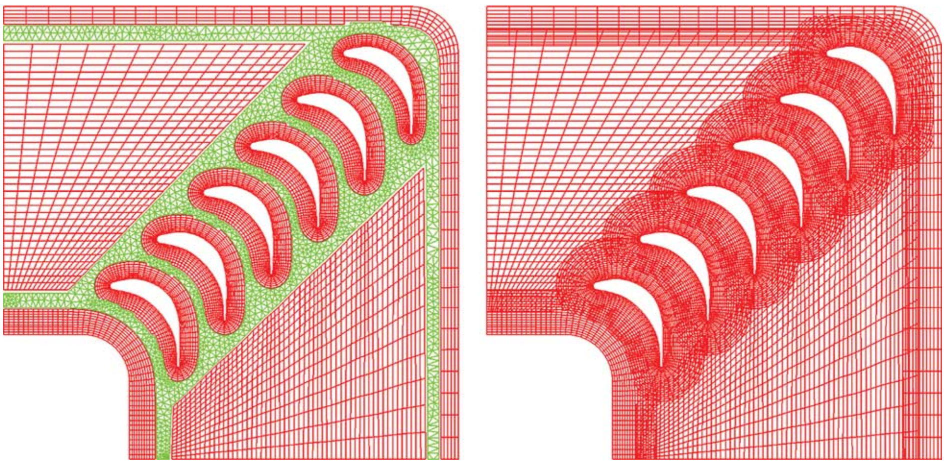

Fig. 26. 3D DRAGON and Chimera grids of the cascade.

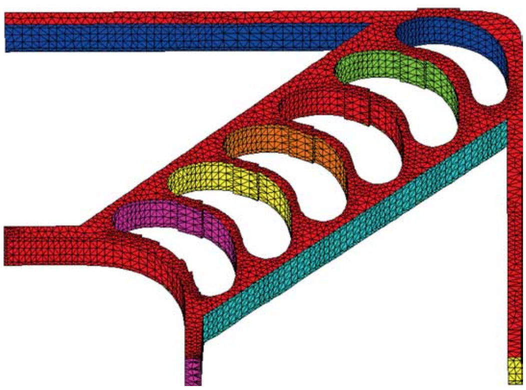

Fig. 27. Unstructured grid of the DRAGON grid of the cascade.

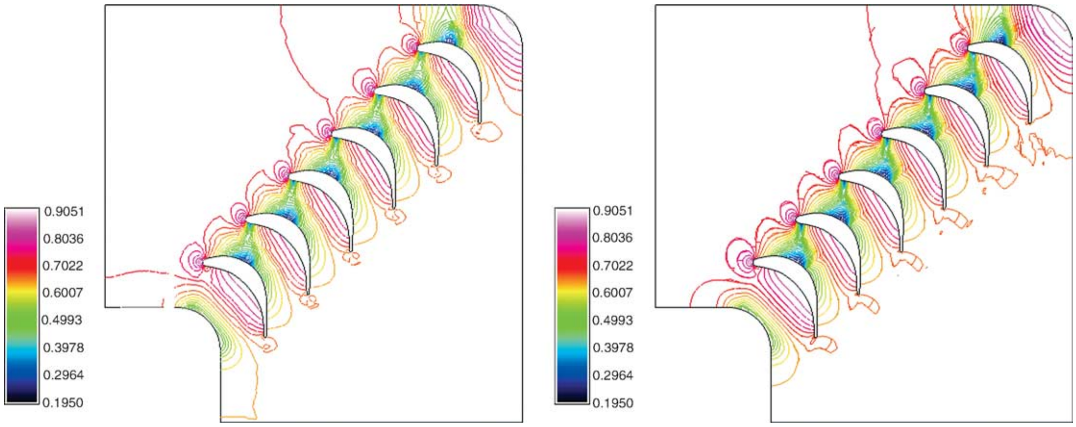

Fig. 28. Pressure distributions of solutions based on the DRAGON and Chimera grids.

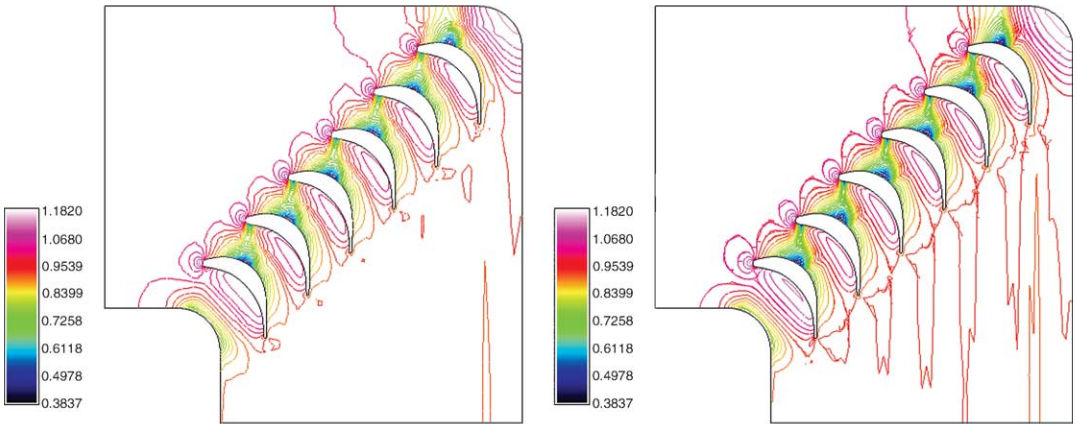

Fig. 29. Density distributions of solutions based on the DRAGON and Chimera grids.

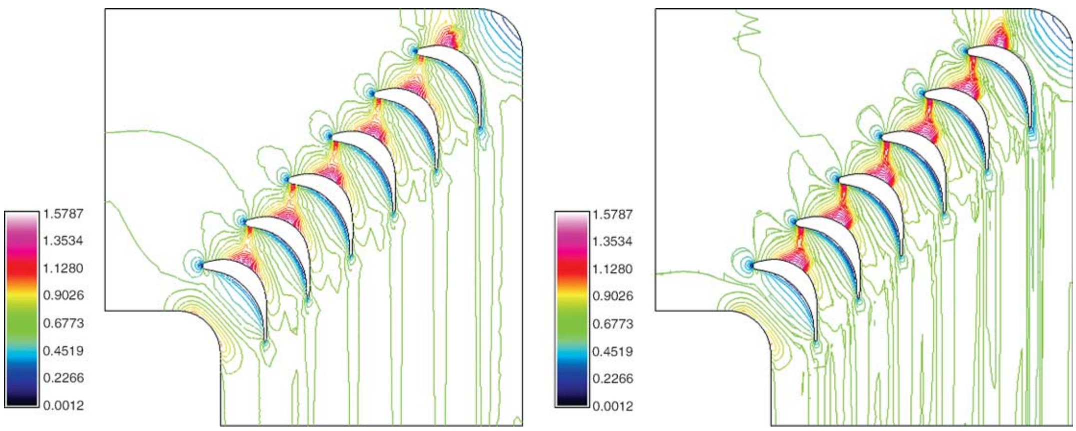

Fig. 30. Mach number distributions of solutions based on the DRAGON and Chimera grids.

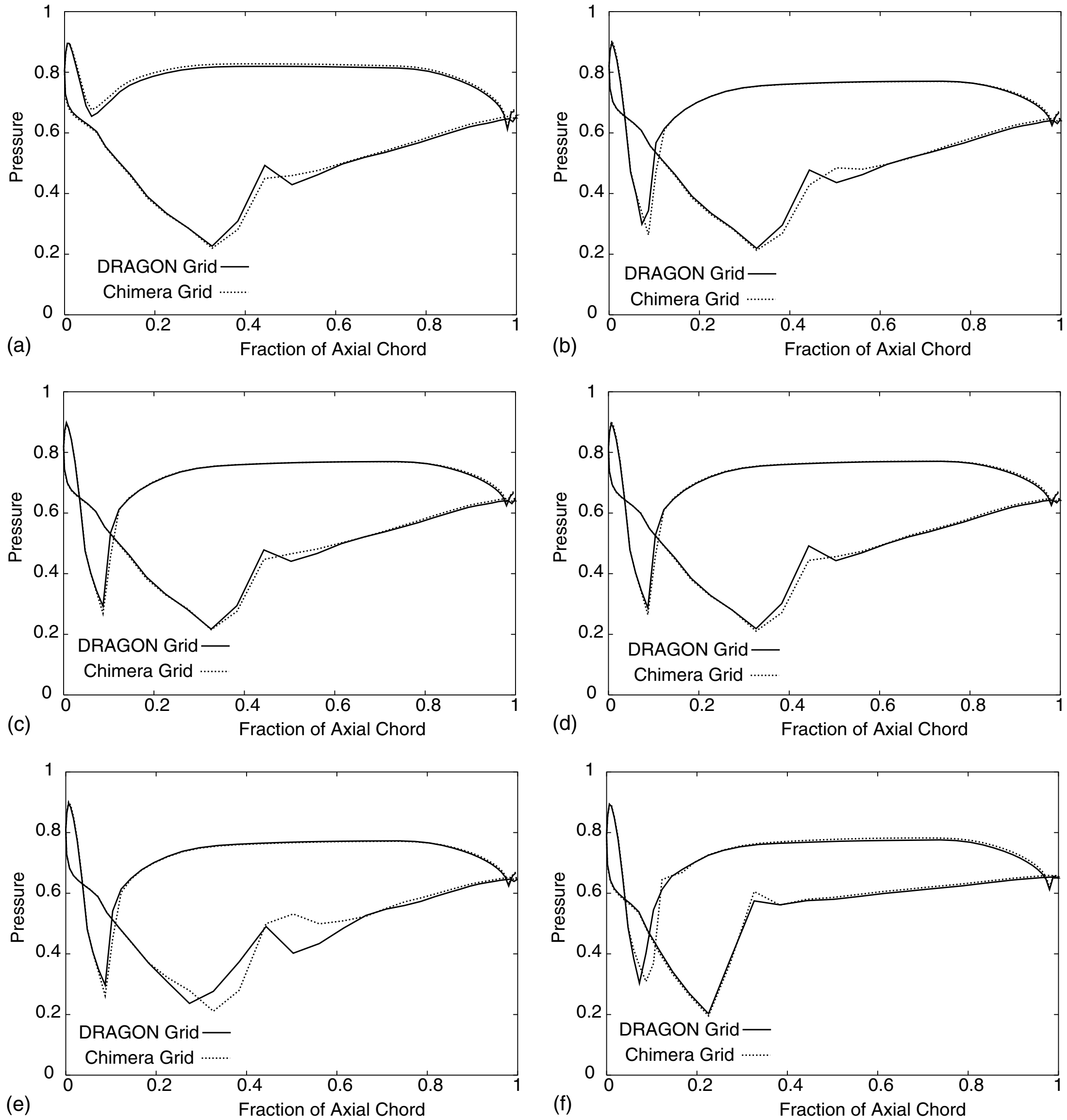

Fig. 31. Pressure distributions around the six vanes: (a)–(f) are for the first to last vanes from the center outwards, respectively.

computational domain of concern, and Fig. 27 shows the unstructured grid of the corresponding DRAGON grid. Figs. 28–30 depict the pressure, density and Mach number contours of the solutions. Finally Fig. 31 shows the pressure distributions on the surfaces of the six vanes, where (a)–(f) are for the first to last vanes from the center outwards, respectively. While no measurements are available for comparison, both Chimera and DRAGON grid solutions, at least serving as a code-to-code validation, are in agreement with each other, especially on the pressure side of the vanes. But there are noticeable differences on the suction side of the vanes. From the contour plots, Figs. 28–30, the DRAGON grid solutions appear to be smoother and free of noises emanating from the interpolation surfaces.

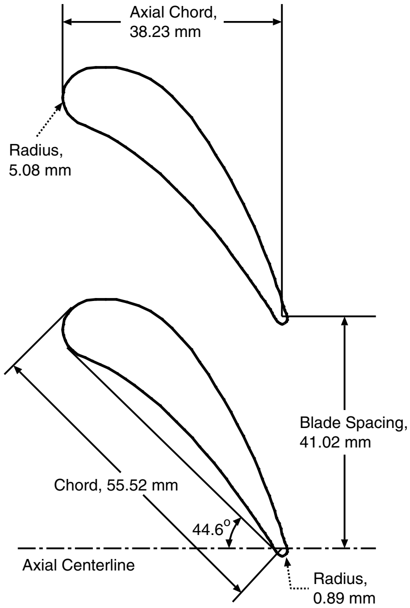

Fig. 32. Core turbine stator vane geometry at the mean section.

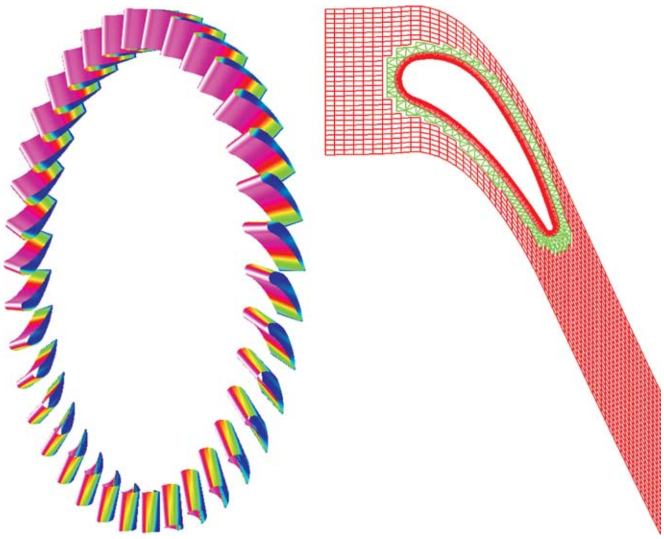

Fig. 33. 3D DRAGON grid for a turbine vane.

5.2. Viscous flow through an annular cascade

Lastly, we show the results of a flow simulation for an annular cascade of turbine stator vanes developed and tested at NASA Lewis [6]. The annular ring has 36 untwisted vanes, of constant profile from hub to tip, with a hub-tip radius ratio of 0.85 and a tip diameter of 508 mm. The vanes themselves are 38.10 mm high, and have an axial chord of 38.23 mm and a blade chord of 55.52 mm (see Fig. 32). Design flow conditions

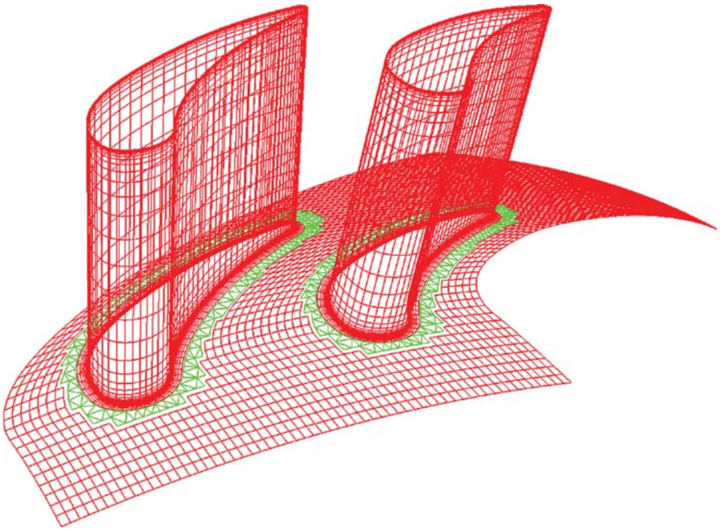

Fig. 34. DRAGON grid of the annular turbine cascade.

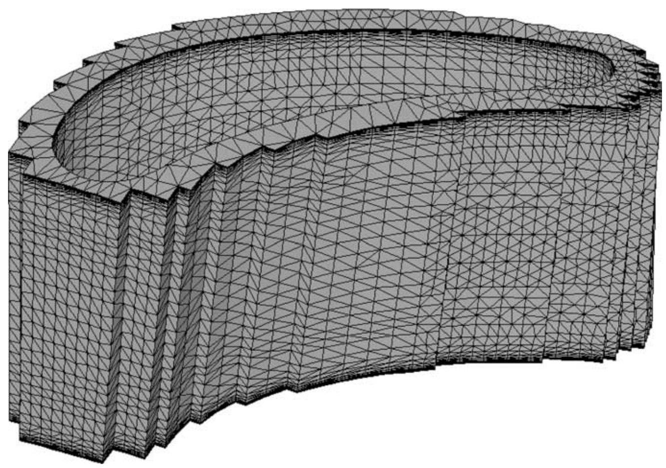

Fig. 35. Unstructured grid of the corresponding DRAGON grid.

are for a fully axial inflow with an exit-hub-static to inlet-total pressure ratio of 0.6705. The designed inflow Mach number is 0.2. The Reynolds number based on the axial chord is 1.73×10^5 [3], or 4.52524×10^6 in a unit of meter used as an input value for the solver. These conditions correspond to average inlet and exit Mach numbers of 0.211 and 0.697, respectively. However, as in [3] we assume the free stream Mach number of 0.2 in the calculation.

A DRAGON grid as shown in Figs. 33 and 34 is used for the flow simulation. It consists of a background H-type grid placed to cover the channel between the vanes, an O-type viscous grid used to resolve the region around the vane, and an unstructured grid (see Fig. 35) located in the overlapping region between the H- and O-type grids. The H-type grid has $60\times31\times33$ points, and O-type grid $85\times20\times33$ points. All the three component grids have viscous layers near the hub and the tip. The initial spacing at the wall is 0.0002 of a blade chord, that is, 0.0111 mm.

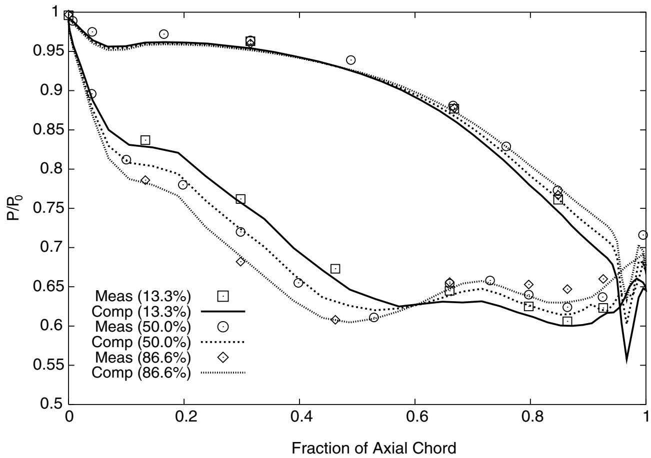

Fig. 36. Computed and measured static pressure distributions at 13.3%, 50% and 86.6% of span from hub.

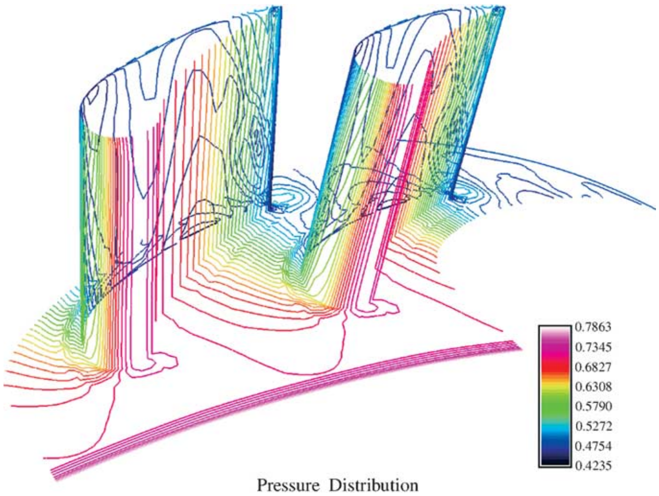

Fig. 37. Pressure distribution for the annular turbine cascade showing two vanes.

Previous calculations have been obtained using a single structured grid [2,3]. The computed surface static pressure distributions of the present DRAGON grid solution are plotted in Fig. 36, and they are seen to be in very good agreement with the measured data [6] at three spanwise locations, 13.3%, 50%, and 86.6%, respectively. Note that the plot shown in Fig. 36 has been scaled with respect to the inlet-total pressure P_0. Fig. 37 depicts the pressure contours on the vane surfaces and on the hub. The pressure side displays a basically two-dimensional behavior while a significant spanwise variation is seen on the suction side.

6. Concluding remarks

In the present work, we have concentrated on the extension of the DRAGON grid method into three-dimensional space. This method attempts to preserve the advantageous features of both the structured and unstructured grids, while eliminating or minimizing their respective shortcomings. The flow solutions confirm the satisfaction of conservation property through the interfaces of structured–unstructured regions, and the results are in very good agreement with the measured data, thus demonstrating the reliability of the method. Future plan includes further validations and applications to engineering problems with complex geometry.

Acknowledgement

We thank R.V. Chima for providing the vane geometry of the annular cascade.

References

[1] P.G. Buning et al., OVERFLOW user's manual, version 1.8f, Unpublished NASA report, NASA, 1998.
[2] R.V. Chima, P.W. Giel, R.J. Boyle, An algebraic turbulence model for three-dimensional viscous flows, NASA TM 105931, NASA, 1993.
[3] R.V. Chima, J.W. Yokota, Numerical analysis of three-dimensional viscous internal flows. NASA TM 100878, NASA, 1988.
[4] N.T. Frink, Upwind scheme for solving the Euler equations on unstructured tetrahedral meshes, AIAA J. 30 (1) (1992) 70–77.
[5] N.T. Frink, Tetrahedral unstructured Navier–Stokes method for turbulent flows, AIAA J. 36 (11) (1998) 1975–1982.
[6] L.J. Goldman, R.G. Seasholtz, Laser anemometer measurements in an annular cascade of core turbine vanes and comparison with theory. NASA Technical Paper 2018, NASA, 1982.
[7] M.-S. Liou, A continuing search for a near-perfect numerical flux scheme, Part I: AUSM$^+$. NASA TM 106524, Lewis Research Center, Cleveland, Ohio, 1994. Also J. Computat. Phys. 129 (1996) 364–382.
[8] M.-S. Liou, Numerical speed of sound and its application to schemes for all speeds, AIAA Paper 99-3268-CP, 14th AIAA CFD Conference, 1999.
[9] M.-S. Liou, C.J. Steffen, A new flux splitting scheme, J. Computat. Phys. 107 (1993) 23.
[10] M.-S. Liou, Y. Zheng, Development of 3D DRAGON grid method for complex geometry, in: D.A. Caughey, M.M. Hafez (Eds.), Frontiers of Computational Fluid Dynamics—2002, World Scientific Publishing Company, Singapore, 2001, pp. 299–317.
[11] M.-S. Liou, Y. Zheng, A three-dimensional hybrid grid: DRAGON grid, in: N. Satofuka (Ed.), Computational Fluid Dynamics 2000, Proceedings of the First International Conference on Computational Fluid Dynamics (1st ICCFD) (Kyoto, Japan, July, 2000), Springer-Verlag, Berlin, 2001, pp. 113–118.
[12] M.-S. Liou, Y. Zheng, A flow solver for three-dimensional dragon grids. NASA TM 2002-211512, NASA, May 2002.
[13] Y. Zheng, M.-S. Liou, Progress in the three-dimensional DRAGON grid scheme. AIAA Paper 2001–2540, Presented at the 15th AIAA Computational Fluid Dynamics Conference, California, USA, June 2001.
[14] Y. Zheng, M.-S. Liou, A novel approach of three-dimensional hybrid grid methodology: Part 1. Grid generation, Comput. Methods Appl. Mech. Engrg. 192 (35–36) (2003), preceding article in this issue.
[15] Y. Zheng, M.-S. Liou, K.C. Civinskas, Development of three-dimensional DRAGON grid technology. NASA TM 1999-209458, NASA, November 1999.